Received: 21 January 2022 | Revised: 21 April 2022 | Accepted: 18 May 2022

DOI: 10.1111/jace.18619

Journal of the American Ceramic Society

RESEARCH ARTICLE

Quantitative inspection of grain-scale chemical inhomogeneities in high-entropy AlB_2-type transition metal diborides

Frédéric Monteverde[1] | **Federico Saraga**[1] | **Mattia Gaboardi**[2] | **Lun Feng**[3] | **Gregory Hilmas**[3] | **William Fahrenholtz**[3]

[1]Institute of Science and Technology for Ceramics–National Research Council of Italy, Faenza, Italy

[2]Elettra-Sincrotrone Trieste S.C.p.A, Basovizza, Trieste, Italy

[3]Missouri University of Science and Technology, Rolla, Missouri, USA

Correspondence
Frédéric Monteverde, Institute of Science and Technology for Ceramics–National Research Council of Italy, Via Granarolo64, I-48018 Faenza, Italy.
Email: frederic.monteverde@istec.cnr.it

Funding information
Elettra-Sincrotrone Trieste, Grant/Award Number: Proposalnumber-20200101; U.S. National Science Foundation, Grant/Award Number: CMMI-1902069

Abstract

The chemical homogeneity of single phase high-entropy AlB_2-type Ti-Zr-Hf-Ta-TM diboride (TM = Cr, V, W, Mo), as well as Ti-Zr-Hf-Mo-W solid solutions was investigated using a new method based on the comparative examination of information provided by electron microscopy and structural parameters. The study of the densification behavior was accomplished, and strong correlations among densification rate-grain coarsening-long range chemical randomization were found. High-resolution synchrotron radiation X-ray diffraction supported by grain-scale chemical analyses by energy dispersive spectroscopy indicated that homogenization of the metals was incomplete, with direct impact on the refined lattice μ-strain. The chemical inhomogeneity was on the same length scale as the grain size, which makes it hardly detectable by typical chemical mapping using energy dispersive spectroscopy. Based on this analysis, the resulting μ-strain broadening is not an intrinsic property of the material, but strongly depends on its processing history.

KEYWORDS

EDS, high-entropy ceramics, lattice μ-strain, Rietveld refinement, SEM, synchrotron radiation XRD

1 | INTRODUCTION

The "supremacy of diversity," as recently suggested by Y. Sun and S. Dai can be unlocked by leveraging entropy of mixing, which is a measure of the randomness of configurations.[1] For solids, higher entropy should result in more stable compounds. In high entropy (HE) materials, disorder is achieved by using multiple elements of similar valence/charge but dissimilar size that are randomly dispersed on degenerate sites in the crystal structure.[2] With the right compositions, elements of different sizes distort the structures without disrupting them. Lattice distortion has been proposed to lead to interesting properties, many of which can be beneficial.[3,4] HE materials might be alternatively termed multi-component, multi-principal element, or even compositionally complex materials,[5] but the high-entropy epithet has stuck in the first seminal literature and survived to date in this area of a rapidly

rising scientific production.[4] The HE materials and the entropy stabilization effect were first investigated in metallic alloys consisting of five or more metals in equimolar proportions.[6] Perhaps more than 40 metals in the periodic table of the elements could provide desirable properties, leading to an enormous number of possible combinations of five elements or more in equal amounts, thus promising an immeasurable number of new materials.

Among the HE materials, HE ceramics (HECs) came to prominence in 2015 when the entropy stabilization of a five-element rocksalt-type equimolar (Mg,Ti,Cu,Zn,Ni)O phase was experimentally documented.[7] Since then, other classes of HECs like borides, carbides, and nitrides attracted the attention.[2–5] Browsing through the diverse HECs, a new group of ultrahigh temperature ceramics (UHTCs) first published in 2016 with the synthesis and fabrication of HE diborides,[8] are among the materials being explored for a spectrum of high-tech applications ranging from thermal/environmental barrier-coatings to catalysts and water splitting, as well as hard and wear resistant coatings or next generation nuclear shielding materials.[2–4,9] UHTCs represent a cutting-edge class of high performing materials, having melting temperatures above 3300 K and consisting of a small number of borides, carbides, and nitrides of early transition metals (TMs), such as HfB_2, ZrB_2, HfN, and TaC. UHTCs were proven to be useful in wide-ranging technologies and are currently studied as key-enabling technologies capable of withstanding extreme environments that are beyond the capabilities of existing structural materials.[10] Since then, many investigators have joined the effort to discover new materials by exploring an uncharted compositional space characterized by a virtually boundless number of combinations. The last five years have seen an extraordinary growth in the number of papers/reviews on HECs.[2,3,5,10] Among the new high entropy UHTCs that emerged, the borides that contain five or more group IV-V-VI TMs in a single crystalline phase have attracted substantial interest. The site occupancy of HE borides has been assumed to be random, but the present work is the first to probe metal distribution systematically.

While solid solutions are often assumed to result in properties that are an average of its constituents, HE diborides have often demonstrated enhanced properties that exceed predictions based on linear rule-of-mixture estimates. The most striking result pertains a well-documented leap in hardness,[11,12] which suggests that the increase in chemical disorder results in deformed lattices and the shear strains that are the key difference between low- and HE materials. Therefore, the full randomization of the chemical elements across *all spatial scales* is of paramount importance because it distinguishes a HE material from low-entropy and multiphase material.[12]

The assessment of the full randomization across all scales, very often accompanied by an a priori assumption of equimolar shares, has received little attention, supposedly due to the unavailability of appropriate analytical tools. Achieving complete randomization of the principal metallic species in HECs strongly depends on the processing history, in particular (but not exclusively) by the duration of the synthesis/sintering steps at the maximum applied temperature and pressure. In other words, the specific combination of elements along with the experimental conditions during synthesis may lead to HECs where compositional homogeneity may not have been achieved.

Previous studies of HE borides have assumed that compositional homogenization was reached after synthesis/sintering, that metal distribution was random across all scales (i.e., from short to large scale range), and that the metallic species were present in ideal equimolar proportions.[13–24] Some authors acknowledged deviations from equimolar metal ratios but have stood by the assumption of overall long-range chemical homogeneity.[20–22,25] Qin M. and coworkers studied a series of dual-phase HE UHTCs using Ti, Zr, Hf, Ta, and Nb as principal element.[20] They used scanning electron microscopy–energy dispersive spectroscopy (SEM-EDS) mapping to assess metallic homogeneity at the micrometer level of a *quasi-equimolar* composition $(Ti_{0.22}Z_{0.19}Nb_{0.18}Hf_{0.19}Ta_{0.19}W_{0.03})$ B_2. Their ceramics contained residual (but not negligible) amounts of W, which was introduced during processing with WC milling media. A homogeneous elemental distribution was also reported by Zhang et al.[21] who identified five metallic species, although not in perfect equimolar proportions, in $(Ti_{0.19}Zr_{0.19}Cr_{0.19}Hf_{0.2}Ta_{0.22})B_2$. Again Zhang et al.[22] reported a measurable deviation from equimolarity (e.g., $Ti_{0.21}Zr_{0.28}Mo_{0.18}Hf_{0.21}W_{0.13}B_2$ when Cr and Ta were replaced by Mo and W). The lack of W in the primary HE diboride matrix was due to the formation of a $(W_{0.58}Mo_{0.28}Zr_{0.15})B$ as an impurity phase, where part of the W needed to reach a quasi-equimolar ratio got segregated into the new monoboride phase. Another TM, Nb, which is frequently used in combination with Ti, Zr, Hf, and Ta, was shown to segregate within a microstructure of single phase $(Ti,Zr,Nb,Ta,Hf)B_2$ solid solutions by means of SEM-EDS elemental mapping.[14,16,22,25]

The present study employs six dense and nominally single phase HEB solid solutions (SS) containing five transition metals with the intent of specifically addressing the long-range compositional fluctuations in the single $(Ti, Ta, Zr, Hf, TM)B_2$, TM = Nb/Cr/V/Mo/W, or $(Ti,Zr,Hf,Mo,W)B_2$ phases. The HEBs have microhardness values high enough to be considered super-hard.[11] To achieve this goal, the lattice μ-strain (Lμ-S) is adopted as descriptor to quantify the long-range chemical

homogeneity. The reason for this choice is based on the direct relation between the average lattice parameters expected from a specific composition and its chemical structure. While in the case of a phase containing a single transition metal, such as ZrB_2, only a single set of lattice parameters (that is, a and c) is expected with very narrow peaks in the powder diffraction pattern. In contrast for high-entropy systems, every fluctuation in the chemical composition will give rise to a different set of lattice parameters, which broadens the diffraction peaks. In the present case, each crystalline grain can have such a fluctuation around the average composition. More details about the origin of microstrain in powder diffraction can be found elsewhere.[26] In the present study, high resolution synchrotron radiation (SR) X-ray diffraction analysis, and field emission SEM-EDS elemental mapping were jointly used to establish a direct relation between larger Lμ-S and the increasing inhomogeneity of mixing of the principal TMs. A statistical approach was implemented to study the compositional fluctuations and detect chemical texture as a spatial recursive arrangement due to different TM concentrations.

2 | EXPERIMENTAL METHODS

Six different compositions were explored and labeled as follows:

HEB-Cr: (Ti, Zr, Hf, Ta, Cr)B_2

HEB-V: (Ti, Zr, Hf, Ta, V)B_2

HEB-Nb: (Ti, Zr, Hf, Ta, Nb)B_2

HEB-W: (Ti, Zr, Hf, Ta, W)B_2

HEB-MoW: (Ti, Zr, Hf, Mo, W)B_2

HEB-Mo: (Ti, Zr, Hf, Ta, Mo)B_2

Powders were prepared by a two-step boro/carbothermal reduction process as described in our previous studies.[27] The partially reacted diboride powders were synthesized at 1650°C. Densification was accomplished at 2000°C or 2100°C, for 10 min by spark plasma sintering (SPS, DCS10, Thermal Technology) under mild vacuum (~2 Pa) and a final applied uniaxial pressure of 50 MPa. The materials HEB-Cr, HEB-Mo, and HEB-MoW were densified at 2000°C, while HEB-V along with HEB-W and HEB-Nb at 2100°C. The furnace cooled to 1000°C at 50°C/min and under a uniaxial pressure of 25 MPa and then cooled at the natural furnace rate to room temperature. More experimental details are reported elsewhere.[11] The linear shrinkage (dL) during SPS was analyzed by recording the displacement of the upper punch (±0.01 mm accuracy). The linear shrinkage was also recorded with no sample inside the graphite die (dL_C) under the same conditions used when the die was filled with powder: The dL_C versus time baseline curves were thus obtained and used to remove the raw dL signal that resulted from thermal expansion of the graphite fixtures during heating.

Densification curves were calculated from the corrected linear shrinkage (dL_F) obtained during SPS after subtracting the contribution of thermal expansion (dL_C) of the graphite fixtures $dL\ (t) = dL_F(t) + dL_C(t)$. Equation (1) describes the corrected displacement at the end of the second isothermal dwell:

$$rd\ (t) = \frac{rd_F \times z_F}{[z_I - dL_F\,(t)]} \tag{1}$$

where $z_I = z_F + dL_{F,MAX}$ was used to convert dL_F into the relative density rd(t), z_I and z_F being the thickness of the sample, respectively, before and after sintering. $dL_{F,MAX}$ is the corrected full excursion of the upper piston at the end of the second isothermal dwell. The mass of powder pressed within the two graphite pistons was assumed constant during the various stages of the SPS process (heating and dwells), while the final densification degree was set equal to rd_F. Sintered pellets, 20 mm outer diameter and about 1.5 mm final thickness, were ground on both sides to remove the graphite foil and any reaction layers. Then, a thin slice was cut from each sintered pellet and halved: one half was polished to a 0.25 μm finish for electron microscopy analyses, the second half was prepared as sample for X-ray powder diffraction (XRPD) analysis. The thin slice was put inside a stainless-steel die (inner diameter 20 mm) and was crushed into small fragments by hammering a stainless-steel piston (20 mm outer diameter) inserted inside the die. The fragmented pieces were sieved (400 μm mesh screen). Then, a strong magnet was used to remove any metallic debris from the fragmented pieces. Successively, the fragments were ground more finely using a zirconia pestle-mortar tool to reach the desired mesh size of about 150 μm. Microstructures of the sintered materials were analyzed using a field emission scanning electron microscopy (FESEM, ZEISS Σigma–Germany) with in situ chemical analysis by energy dispersive spectroscopy (EDS, INCA Energy 300 detector, Oxford Instruments–UK). The residual amounts of the unreacted reducing agents were estimated by analyzing FESEM micrographs of polished cross sections acquired in backscattered secondary electron (BSE) mode using computerized image analysis program (Image Pro Plus 6, Media Cybernetics, US): at least three micrographs per specimen were counted. The increased intensity of the accelerated electron beam (more than 1 pA at 15 keV of energy) enhanced the overall contrast and, therefore, the composition contrast. Elemental maps were acquired through FESEM-EDS analysis: the beam energy generally set to 20 keV unless otherwise

stated in the text. A quantitative determination of the overall metal concentrations in the sintered specimens was also accomplished using an energy dispersive X-ray fluorescence spectrometer (EDXRF, mod. S2 PUMA, Bruker) using one 20 mm diameter surface of the sintered disc.

Synchrotron radiation X-ray powder diffraction (SR-XRPD) data of the as-pulverized materials were collected on the high-resolution MCX beamline at the Elettra synchrotron light-source (Trieste, Italy) with $\lambda = 0.7293$ Å (17 keV). The instrument profile was calculated using a standard reference material (Si, SRM 640c, National Institute of Standards and Technology) by refining the peaks shape with the pseudo-Voigt (PV) function available in the GSAS-II suite.[28] It is worth mentioning that silicon has a null microstrain broadening and negligible size broadening. Borosilicate capillaries (0.2–0.3 mm diameter) were filled with the pulverized samples and the diffraction patterns were acquired at room temperature in Debye–Scherrer geometry on the 4-circle Huber goniometer by spinning the capillary at 300 rpm. Data were then analyzed by means of Rietveld refinement starting from the AlB_2-type structural model, space group P6/mmm. The uniaxial Lμ-S profile correction was required to accurately fit the anisotropic peak broadening (PB) present in all the six samples.

Bulk densities (r_B) were measured according to the ASTM C373 standard test method.[29] Theoretical densities (r_{TH}) were calculated using Equation (2):

$$r_{TH} = \frac{Z \times M}{N \times V_{XRD}} \quad (2)$$

where Z and M are, respectively, the number of atoms in the unit cell and their molecular weight, N is Avogadro's number, and V_{XRD} the lattice volume of the sample obtained from the pulverized sintered material. V_{XRD} was calculated using the cell parameters obtained by Rietveld refinement, while M was calculated using the TM contents provided by quantitative FESEM-EDS. The boron-to-TM atomic ratio in the six materials was assumed equal to 2. Back-scattered electron (BSE) imaging mode was preferred to collect SEM images and visualize individual grains. The chemical composition (fluctuations included) was determined through extensive FESEM-EDS elemental mapping (MAP) acquisitions. The quantitative mapping generated the distribution of concentration for each TM that was present in the material: such datasets were also used to perform a chemically related texture analysis with a statistical approach. A detailed description of the statistical method is reported in the Results section and represents an important outcome of the present work. The grain size data (mean ±1 standard deviation) were retrieved from reference.[11]

3 | RESULTS

3.1 | High-resolution SR-XRPD analyses

SR-XRPD patterns and relative Rietveld refinement of the six as-pulverized samples are presented in Figure 1 with a logarithmic scale to highlight the absence of minority phases. Each pattern can be entirely described by the presence of a single hexagonal (AlB_2-type) phase. The absence of residual unindexed peaks suggests that the mechanical pulverization of the thin slice did not produce any extrinsic contamination. For some of the patterns, the first three peaks in the 2-theta range 10°–20°, respectively the 001, 100, and 101 peaks, display anisotropic broadening (i.e., in this case, different broadening from one crystallographic direction to the orthogonal one).

This effect is normally found in powders of crystallites exhibiting small domain-size and/or lattice μ-strain effects. Since these two effects have different angular dependencies, separation is possible, which avoids correlations in the fitting procedure. As a result, size-broadening could be dismissed (domains were larger than 1–2 μm and had a negligible effect on the profile), which allowed direct analysis of the lattice μ-strain. The output is summarized in Table 1.

To avoid uncontrolled correlations during the least mean square fitting, the atomic occupancies of the TMs were maintained at the values dictated by FESEM-EDS analyses (see Table 2). The atomic ratios reported in Table 2 were normalized to 100% and based on averages of at least three areas of about 10^{-2} mm2. The maximum relative error connected to the mean atomic amounts of various TMs does not exceed 0.5 at%.

3.2 | Microstructure

Polished surfaces were used to analyze the long-range microstructure of the six materials. A representative BSE micrograph for each composition is shown in Figure 2, while in Table 3, some important characteristics of the as-sintered materials are reported.

The change of just one/two principal elements among the TMs of the starting composition gave rise to evident differences in the final microstructures. BSE-FESEM image analyses provided an estimate of the final amount of porosity (p) as well as of the residual unreacted precursors (boron carbide and carbon) used for the boro/carbothermal reduction reactions.[27] The bright contrast outlining a darker spot is a feature typical of an empty pore especially when a very intense electron beam hits the polished sample surface and enhances the so-called

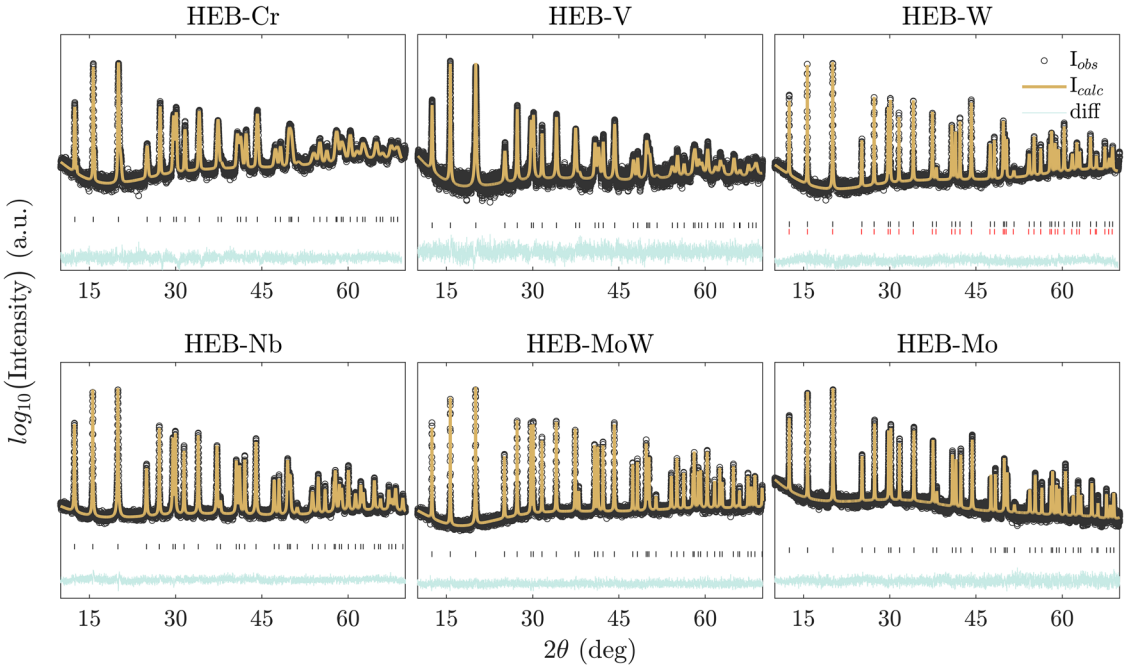

FIGURE 1 High-resolution synchrotron radiation XRPD data and Rietveld refinements.

TABLE 1 Refined parameters (errors in parenthesis): cell parameters a and c; cell volume V_{XRD}, equatorial- (δ_d/d_{hk0}) and axial-(δ_d/d_{00l}) lattice μ-strain; and weighted R-factor of the refinement (R_{WP})

HEB-xx	a (Å)	c (Å)	V_{XRD} (Å^3)	$\delta d/d_{hk0}$ (%)	$\delta d/d_{00l}$ (%)	R_{WP} (%)
Cr	3.09175(6)	3.3658(1)	27.864(1)	1.444(5)	2.827(25)	7.9
V	3.08631(9)	3.34748(9)	27.614(2)	0.505(3)	1.221(16)	11.4
Nb	3.10546(14)	3.37812(11)	28.217(2)	0.402(4)	0.938(23)	7.7
W	3.09480(2)	3.35246(3)	27.807(1)	0.319(2)	0.929(14)	8.8
MoW	3.08231(3)	3.34464(3)	27.519(1)	0.212(1)	0.597(6)	11.2
Mo	3.09308(1)	3.36093(2)	27.847(1)	0.196(1)	0.433(7)	8.8

TABLE 2 Experimental atomic average-compositions (within 0.5% error) as determined by FESEM-EDS analyses from the average of at least three areas of 10^{-2} mm^2. <TM> is the weighted average of the various TM at%, while M is the molecular weight expressed in atomic mass unit (amu) and used in relation (2)

	HEB-Cr	HEB-V	HEB-Nb	HEB-W	HEB-MoW	HEB-Mo
Ti, at%	19.3	18.7	19.0	19.0	18.6	18.0
Zr, at%	20.3	19.9	19.7	21.0	21.9	19.7
Hf, at%	18.5	20.7	20.5	18.0	18.0	20.1
Nb, at%	—	—	20.1	—	—	—
Ta, at%	20.8	20.5	20.1	20.4	—	19.3
Cr, at%	19.6	—	—	—	—	—
Mo, at%	—	—	—	—	20.8	20.2
V, at%	—	19.1	—	—	—	—
W, at%	1.5	1.0	0.6	21.5	20.7	2.6
<TM>, at%	19.5	19.6	19.4	20.0	20.1	19.0
M, amu	132.98	134.38	141.42	158.44	140.64	143.17

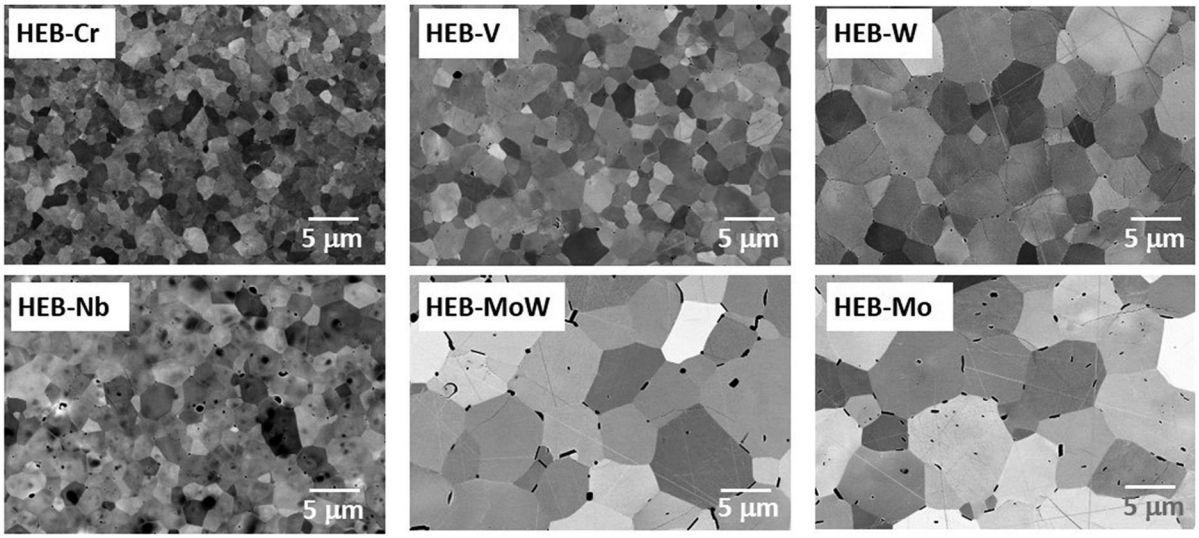

FIGURE 2 BSE-FESEM micrographs from a polished surface, taken at the same magnification. The nature of the black spots in HEB-*x* (*x* = Nb, MoW, or Mo) is described in the main text. Residual scratches due to polishing are still visible in HEB-*x*1 (*x*1 = V, W, MoW, and Mo)

TABLE 3 SPS temperature, bulk density (r_B), theoretical density (r_{TH}), residual porosity (p), final relative density (rd_F), residual volume (R_V) of the unreacted B_4C+C, and mean grain size (mgs) of HEBs

	T_{MAX}	r_B*(±0.01)	r_{TH}(±0.005)	r_B/r_{TH}	p	rd_F**	R_V	mgs(±1st.dev)*
	°C	g/cm^3	g/cm^3	%	%	%	%	µm
HEB-Cr	2000	7.93	7.925	>100	n/i	100	n/i	3.2 ± 1.3
HEB-V	2100	7.88	7.97	98.9	~1	99	n/i	7.7 ± 3.5
HEB-Nb	2100	8.20	8.29	98.9	~1	99	n/i	4.9 ± 2.3
HEB-W	2100	9.45	9.46	99.9	n/i	100	n/i	9.3 ± 3.5
HEB-MoW	2000	8.19	8.485	96.5	~1	99	2.5	13.4 ± 5.5
HEB-Mo	2000	8.22	8.445	97.3	~1	99	1.5	15.9 ± 7.0

n/i, not identified.
(*) from [11]; (**) rd_F = 1-p.

"edge effect." This allows for discrimination of porosity from residual unreacted agents (RV) because the core of a pore or a RV remains dark (compared to the surrounding) while the perimeter of a pore acquires a bright appearance. Figure S2 provides more detailed visual evidence of the edge-effect contrast: In the same Figure S2, an example of an FESEM-EDS elemental mapping is presented. Residual boron carbide and carbon had no measurable effects on the outputs of the SR-XRPD analysis. However, elemental FESEM-EDS analysis allowed us to determine the atomic compositions of the sintered materials, assuming stoichiometric boron content of the TMB_2 compound, with the actual representative chemical compositions reported in Table 2. All six chemical compositions depart slightly from perfect equimolar mixtures in two systematic ways: 1) Ti is constantly below 20 at%; and 2) the presence of W in trace amounts in compositions other than HEB-W and HEB-MoW further deviates the overall composition from equimolarity (if considered as part of the diboride SS). The EDXRF analyses confirmed the experimental ranges of various TMs measured by FESEM-EDS, including a deficit of Ti, and contamination from W. With the exception of HEB-Nb, SEM imaging (Figure 2) did not reveal evident local segregation in any of the remaining compositions: further long-range FESEM-EDS mapping reported in the following sections definitively excluded the occurrence of local segregation. Nb segregation in $(Hf,Nb,Ta,Ti,Zr)B_2$ is well-documented.[14,16,22,25]. The reasons that an extra phase was not detected in HEB-Nb through SR-XRPD analysis is discussed below. The r_{TH} values were calculated, according to Equation (2), using the experimental values of V_{EXP} (see Table 1) and M (see Table 2). The calculated r_B/r_{TH} ratio is consistent with the final relative density (rd_F) of the as-sintered material, rd_F = 1-p, when the reducing agents, initially added to the oxide blend, were fully consumed. Traces of unreacted B_4C and C are still visible in Figure 2 mainly as black elongated spots. Ceramics containing Mo also contained a few percent of RV, which led to

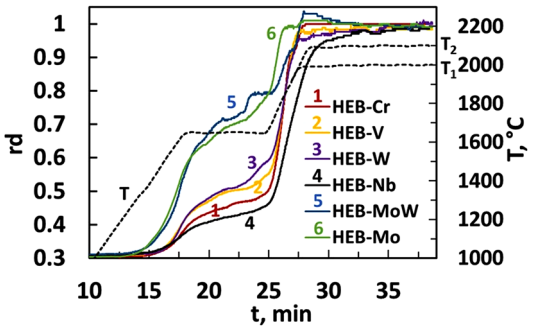

FIGURE 3 Relative density (rd) versus time (t) calculated using relation (1): the second dwell was set at $T_1 = 2000°C$ (curves 1,5,6) or $T_2 = 2100°C$ (curves 2,3,4)

the discrepancy between r_B and r_{TH}. The calculation of the densification curves versus time was made using rd_F values reported in Table 3 as input for the final relative density.

3.3 | Densification behavior

The densification curves were calculated with Equation (1) and are plotted in Figure 3. A more detailed visualization of the rd variation versus time of the isothermal stages is presented in Figure S3. The comparison of densification curves enables assessment of whether a particular combination of TMs promotes full density simply by adjusting the peak SPS temperature (see Table 3). For HEB-Mo, HEB-MoW, and HEB-Cr, a maximum sintering temperature of 2000°C (10 min dwell applying 50 MPa) was enough to achieve $rd_F \geq 99\%$, while an increase of 100°C became necessary to push HEB-V, HEB-W, and HEB-Nb to near full density. The compositions HEB-Mo and HEB-MoW were characterized by the fastest densification rates and stronger grain coarsening based on the values of mean grain size (mgs) in Table 3. Faster densification rates reflected the ability of the specific TM combination to diffuse, which should also favor atomic-level mixing of all the TMs. The materials with increasingly larger mgs, therefore, were hypothesized to have reached a better homogenization. This trend is further supported by the HEB-Nb composition that showed the slowest densification rate, likely due to the hindrance of Nb to mix homogeneously, which resulted in the widespread Nb segregation that was observed (Figure 2).

3.4 | Long-range fluctuations in chemical composition

A qualitative indication of long-range chemical fluctuations (LRCF) was first observed in the BSE-FESEM images. Image contrast is primarily due to different crystallographic orientations of grains at the surface and is defined enough to allow for measurement of grain sizes. However, more detailed analysis of the BSE-FESEM micrographs shown in Figure 4 provided evidence of additional contrast, superimposed to the orientation contrast, that varied with amplitude and spatial extent. Composition contrast was barely discernible in HEB-Mo and HEB-MoW due to its minor amplitude compared to the other materials, so those micrographs are not displayed. Hence, FESEM-EDS proved useful in the investigation of the long-range chemical fluctuations that can be interpreted as a chemical fluctuation due to a long-range non-ideal mixing of all the principal TMs. To this end, chemical analysis was conducted using FESEM-EDS elemental mapping. A comparative protocol was devised to rank materials possessing different lattice μ-strain as summarized in Figure 5 along with the description below. The FESEM–EDS elemental maps were fragmented in adjacent boxes (Q), each one with diagonal D_Q, chosen based on the actual mgs of the material under investigation. The initial area (A_1) of a the FESEM-EDS elemental map, D_1 being its diagonal, was roughly estimated using the following empirical criterion:

$$A_1 = 1/2{D_1}^2, 0.05 < mgs/D_1 < 0.1 \quad (3)$$

The elemental map was thus built collecting the master spectrum throughout the selected initial area A_1. Post-processing of the master spectrum included defining grids of Q squared boxes (SQB), with diagonal D_Q

$${D_Q}^2 = (\sqrt{2A_1})/Q \quad (4)$$

For each material, the atomic concentrations of various TMs were quantitatively determined by increasing Q up to a certain limit, Q_{MAX}. The Q_{MAX} value was flagged when ½ D_{QMAX} fell below about 1 micron. Overlapping of the probe beam excitation volumes was removed from the analysis of the compositions of adjacent SQBs. Figure S4 provides a graphical guidance to describe the principal steps to obtain a quantitative elemental surface map. The consistency of the compositional homogeneity and fluctuations were analyzed by varying Q from 1 to Q_{MAX}. The descriptor δ_{TM} is defined as,

$$\delta_{TM} = \sqrt{\sum_{i=1}^{N} y_i \left(1 - \frac{x_i}{\bar{x}}\right)^2}, \quad \bar{x} = \sum_{i=1}^{N} y_i\, x_i \quad (5)$$

and it was calculated to address the compositional deviation from the weighted average ($\bar{x}$) inside an individual SQB, with N the number of TMs present with atomic

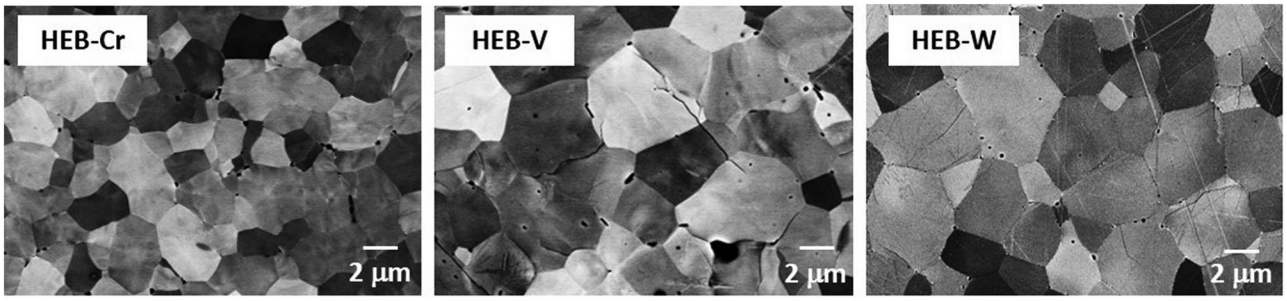

FIGURE 4 BSE-FESEM micrographs from polished surfaces of HEB-TM (TM = Cr, V, or W): The dominating gray levels inside each grain provided by the orientation effect are modulated by a minor component due to a long-range chemical variability. Micro-cracking was also present in HEB-V and HEB-W

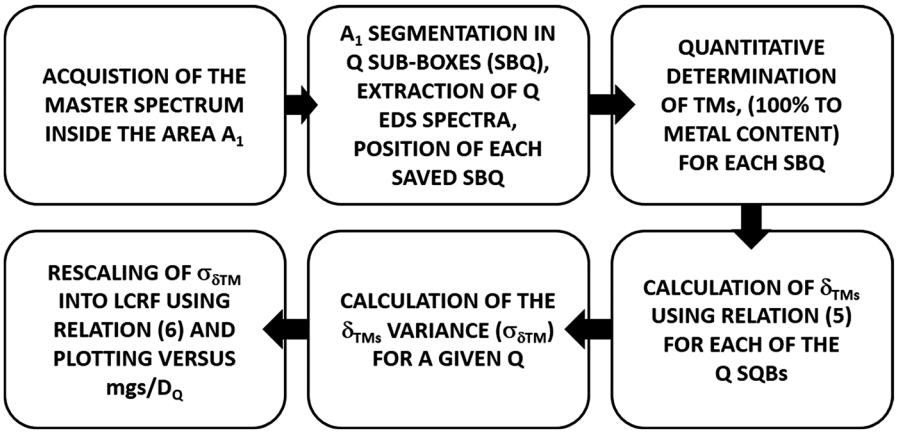

FIGURE 5 Flowchart to calculate the long-range chemical fluctuation LRCF versus mgs/D_Q

concentration y_i ($\sum_{i=1}^{N} y_i = 1$) and relative weight x_i. Larger values of δ_{TM} variance ($\sigma_{\delta TM}$) were interpreted as long-range chemical fluctuations (LRCFs) with stronger intensities, that is, higher deviation from $\bar{x}$. The $\sigma_{\delta TM}$ values were calculated and re-scaled as,

$$LRCF = 1 - \frac{1}{(1+\sigma_{\delta TM})}, 0 \le LRCF \le 1 \qquad (6)$$

The two-fold dependance of LRCF on D_Q and mgs was analyzed as shown in Figure 6. LRCF was plotted as a function of mgs/D_Q to enable direct comparison independent of the actual grain size. The LRCF data for all the six materials are plotted in Figure 7A. The LRCF data were further processed by fitting them to the following power law

$$LRCF = A \times \left(\frac{mgs}{D_Q}\right)^{\frac{3}{2}}. \qquad (7)$$

The goodness of fit values, R^2, were >99.5%. The parameter A was fitted and then plotted versus the average lattice μ-strain <Lμ-S> in Figure 7B. The increasing magnitude, A, matches the experimental increase in <Lμ-S>, defined as:

$$L\mu S = \frac{1}{3}\left(\frac{2\,\partial d}{d_{hk0}} + \frac{\partial d}{d_{00l}}\right), \qquad (8)$$

providing a concise description for the LRCF versus <Lμ-S> trend. In Figures 8 and 9, respectively, the chemical fluctuations in HEB-Cr and HEB-MoW are shown as example of a material with an enhanced or a limited <Lμ-S>. The range over which a variability in the chemical composition appears to be significant turns out to be the same as the grain size, despite differences in orientation of adjacent grains. The compositional fluctuations become negligible when the composition is averaged over areas encompassing dozens of grains.

As a result, the mean values obtained summing up all the data of a single elemental map, as is typically presented as support of chemical homogeneity of high entropy ceramics, do not differ appreciably from the average values reported in Table 2. The range of the mgs/D_Q ratio from about 0.05 to 0.5 was unable to differentiate the chemical fluctuations because the selected length D_Q exceeded

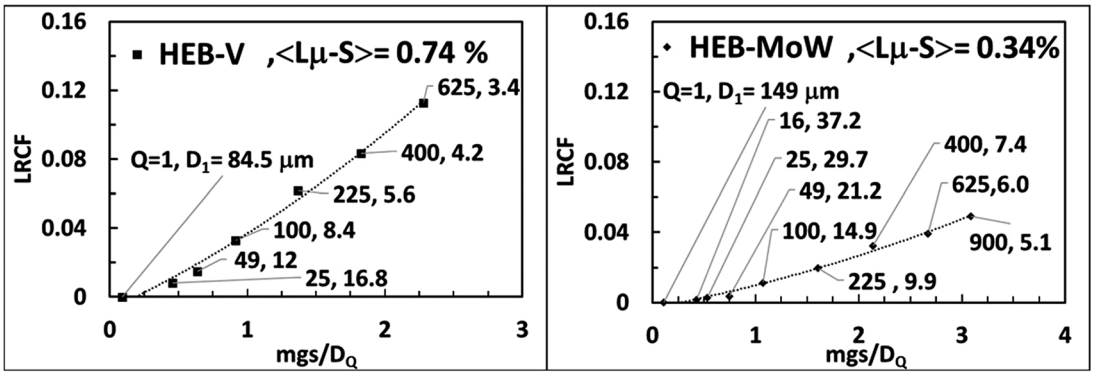

FIGURE 6 Long-range chemical fluctuations (LRCF) versus mgs/D_Q in HEB-V and HEB-MoW as examples showing the Q-D_Q pairs (cfr. Equation (1)) for each experimental point: the DQ unit in μm is omitted for Q >1. The average lattice μ-strains <Lμ-S> are also indicated

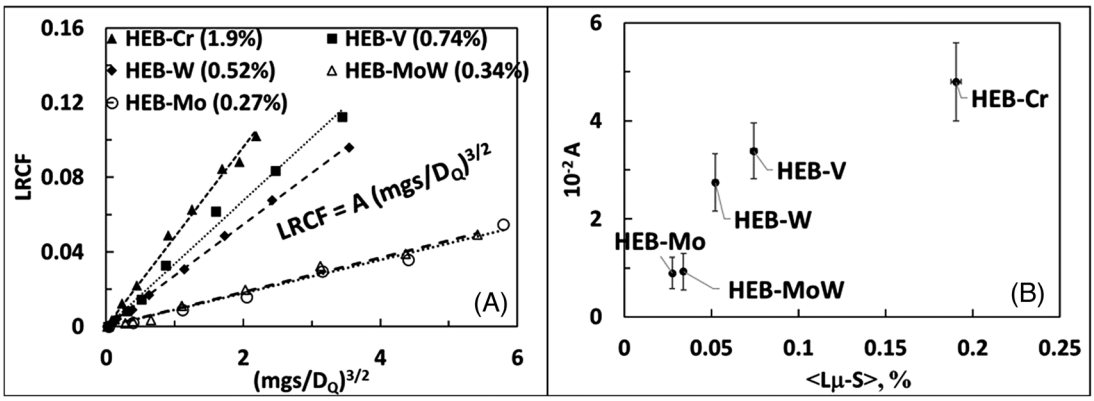

FIGURE 7 (A) Linearization of the long-range chemical fluctuation (LRCF) data versus mgs/D_Q according to the power law $LRCF = A(mgs/D_Q)^{3/2}$; (B) the A parameter versus average lattice μ-strain <Lμ-S>

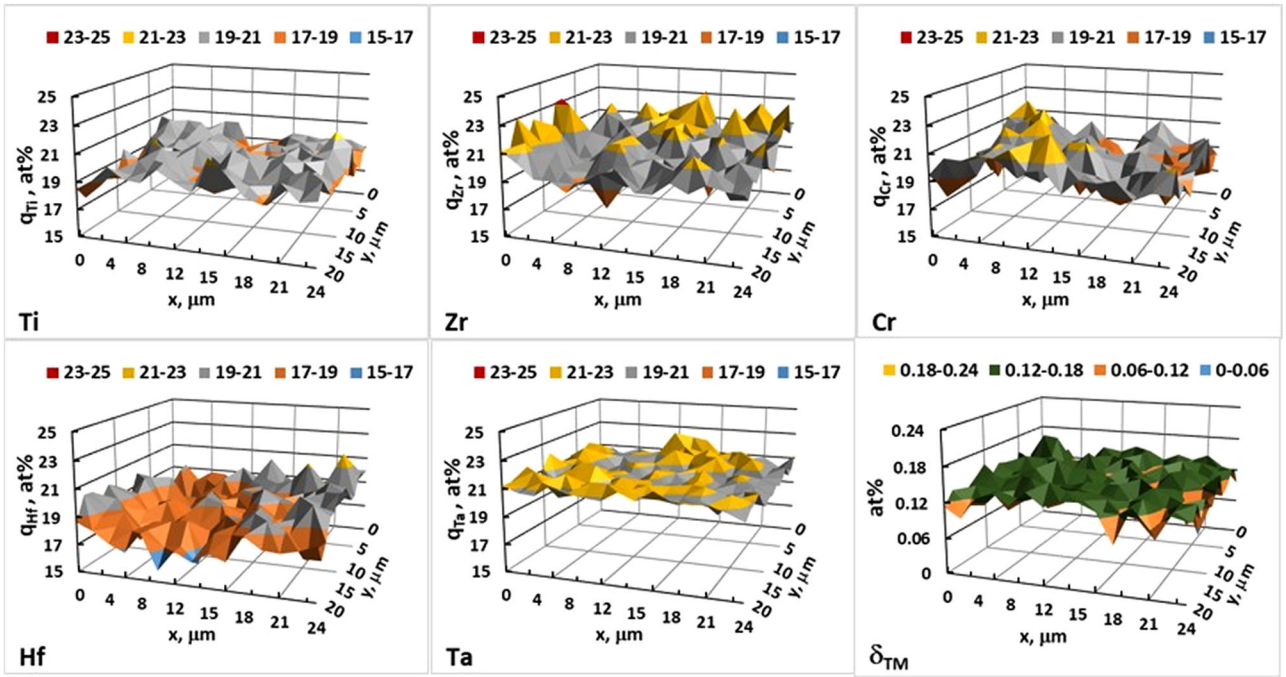

FIGURE 8 Quantitative mapping of HEB-Cr with the atomic percent q_{TM} of various metals (TM) versus linear dimension (x,y) of the mapped area, $\Sigma q_{TM} = 100\%$. The corresponding δ_{TM} descriptor is shown: note that it has a different colored palette than the TM constituents

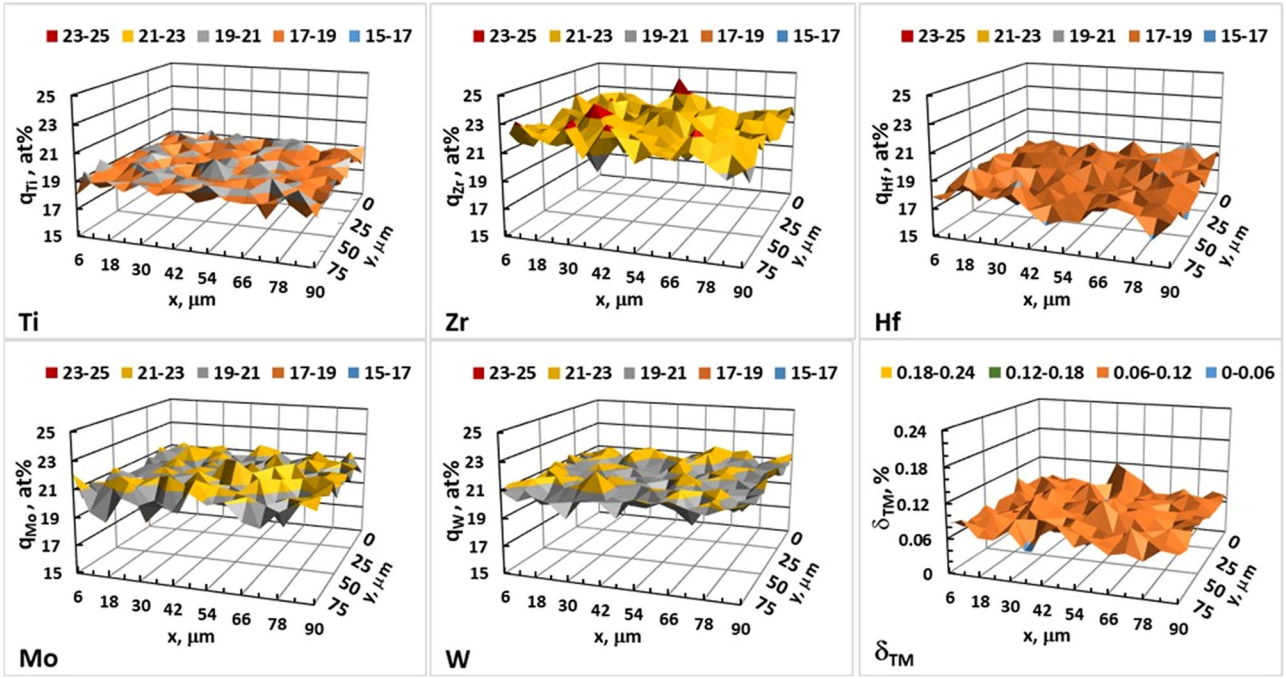

FIGURE 9 Quantitative mapping of HEB-MoW with the atomic percent (q_{TM}) of various metals (TM) versus linear dimension (x,y) of the mapped area, $\Sigma q_{TM} = 100\%$. The corresponding δ_{TM} descriptor is shown: note that it has a different colored palette than the TM constituents

the spatial range over which such fluctuations were significant. When the length scale of the chemical analysis is less than the size of the individual grains, that is, mgs/D_Q ratios of 1 and higher, the chemical inhomogeneities are more evident. For a certain value of mgs/D_Q, higher values of LRCF reflect the occurrence, on average, of an enhanced chemical variability inside individual grains. In addition, the ranking of these materials based on increasing <Lμ-S> matches the order established by LRCF.

3.5 | Long-range chemical texture

In the former section, "Long-range fluctuations in chemical composition" were presented as a method to measure chemical homogeneity and enable correlation of the long-range chemical fluctuations (determined by MAPS) to the lattice μ-strain detected by SR-XRPD. The LRCF values shown in Figure 7A are derived from weighted averages of the TM concentrations, but the spatial arrangements of the SQBs, which segment the squared area A_1 in a regular grid, have no influence over the calculated LRCF. Hence, the overall chemical texture describing a spatial recursive arrangement of the long-range chemical fluctuations is inevitably lost from the analysis. For the actual microstructure, chemical texture can provide information on how frequently the amplitude of the long-range "chemical disorder" varies across a predetermined lengthscale.

A statistical approach inspired by the Haralick method and its impact on the texture analysis was implemented to investigate the chemical related texture.[30] In general, Haralick's texture features are calculated from a gray level co-occurrence matrix (GLCM), a matrix that counts the co-occurrence of neighboring gray levels in an image. The GLCM is a square matrix whose dimension is determined by unreplicated gray levels inside a region of interest. In the present case, the input data to build the co-occurrence matrix were not gray levels of an image, but the δ_{TM} values obtained from the quantitative MAPS. Examples of MAPS were already plotted in Figures 8 and 9 while more case studies are documented in Supporting Information. The δ_{TM} data carry the information into the co-occurrence matrix of the chemical fluctuations (CFCM), if the overall chemical compositions of adjacent areas of a region of interest do not differ appreciably. The Haralick's texture descriptor C_2

$$C_2 = \sum_{i=1}^{k} \sum_{j=1}^{k} \frac{c_{i,j}}{1 + (i-j)^2} \tag{9}$$

is known as the second order inverse difference momentum and typically measures the texture homogeneity over k values, in the present case the unreplicated δ_{TM} values extracted from the MAP. The CFCM brings information about the probability $c_{i,j}$ that two SQBs have the same or dissimilar δ_{TM}. The highest $c_{i,j}$ value along the diagonal

of the CFCM reveals the most recursive δ_{TM} value shared by a pair of adjacent SQBs. As with the analysis described in the long-range chemical fluctuations section, the descriptor RC_2

$$RC_2 = 1 - \left(\frac{1}{1 - C_2}\right), 0 \leq RC_2 \leq 1 \quad (10)$$

is a reformulation of C_2: RC_2 approaching unity (i.e., C_2 tending to 0) is mainly due to the (very low) probability that $c_{i,j}$ along the CFCM diagonal would encounter two adjacent SQBs with the same δ_{TM}. The probability of co-occurrence $c_{i,j}$ cannot be extracted from the δ_{TM} maps without first having predefined a position operator P_1 and its displacement vector $d = (d_x,d_y)$. In Figure S4, the action of the position operator on $d(x,y)$ is shown: the position operator P_1 is described by a displacement vector $d = (1,1)$ in the 0° or 90° directions. As long as P_1 is defined, the frequency of SQB pairs separated by d having chemical disorder $\delta_{TM,i}$ and $\delta_{TM,j}$ can be counted. The CFCM has dimension k^2, where k is the number of unreplicated distinct δ_{TM} values isolated in the MAP. The decisional flow to produce a CFCM matrix is better explained in Figure S6. Maintaining the same operator P_1 but relaxing the difference between two unique δ_{TM} values by imposing a less stringent damping (i.e., increasing the rounding), the $c_{i,j}$ probabilities along the diagonal of the CFCM get higher. This operation of damping the difference between unreplicated δ_{TM} values has a direct impact on the magnitude k^2 of the CFCM matrix, and therefore on the Haralick's texture output. The RC_2 descriptor was calculated according to the following steps.

1. For each material, an outer perimeter of a MAP with area A_1 was chosen so that dozens of individual SQBs, on average, fell well inside the grains, that is, $1.4 \leq mgs/D_Q \leq 1.6$.
2. The area A_1 was the target of FESEM-EDS data acquisition where only one master spectrum was collected.
3. The area A_1 was segmented in a grid of 225 SQBs ($Q = 225$): For each SQB, a δ_{TM} value was calculated and a dataset of 225 δ_{TM} values was produced.
4. The link between δ_{TM} of each SQB and their position inside the area A_1 was recorded.

When the as calculated δ_{TM} values were processed with no rounding, the corresponding CFCM generally showed values of k of 200 or even higher, while the RC_2 descriptor, calculated without any δ_{TM} relaxation, converged to a value indicating a global lack of chemical homogeneity smoothness (i.e., $RC_2 = 1$, cfr. Figure 10A). Increasing the relaxation of the δ_{TM} values from 10^{-4} to 0.1, that is, relaxing the difference between $\delta_{TM,i}$ and $\delta_{TM,i}$ pairs, k decreased significantly for increasing the damping (cfr. Figure 10A). The RC_2 values calculated for increasing rounding (see Figure 10B) show that the materials having less average lattice μ-strain exhibit a steeper decay of homogeneity smoothness RC_2. A thorough discussion of the consequences coming up the texture analysis is referred to the next section. The long-range chemical analyses of HEB-Nb provided meaningless results due to Nb clustering. Hence, HEB-Nb was excluded from Figures 7 and 10.

4 | DISCUSSION

The experimental data and the analytical relationships presented in the Results section support the conjecture that the chemical inhomogeneity of TMs in AlB_2-type high entropy single phase diboride solid solutions can be measured. Inhomogeneity is a result of fluctuations in the concentrations of TMs on the sub-micrometric scale that cannot be detected when the overall chemical composition is calculated across dozens of grains. The present experimental work also proves that this chemical variation that was quantified using precise collection of local chemical data by EDS can also be directly evaluated on a bulk sample using the lattice μ−strain measured with high-resolution XRPD. In addition, the RC_2 descriptor, used to classify the chemical texture intensity (see Figure 10), also ranks the chemical homogeneity of these HEBs with the order established by the average lattice μ-strain determined using SR-XRPD.

The spatial homogeneity of the principal TM species was examined at long (i.e., tenths of micrometers), or short (i.e., some tenths of nanometers) range. Possible effects of such a chemical inhomogeneity on properties (e.g., mechanical properties) was not assessed in the present study but is a topic worthy of future research. To date, only a few dedicated works[31–33] have addressed the chemical homogeneity at *short range* in high entropy materials. These studies concluded that the arrangement of the principal elements was homogeneous and random. Rost et al. explored entropy-stabilized oxides in the (Mg, Co, Ni, Cu, Zn) O cubic system and through rigorous analysis mediated by X-ray diffraction, extended X-ray absorption fine structure (EXAFS) and scanning transmission electron microscopy (STEM)-EDS concluded that the cations were uniformly dispersed.[7] B. Jiang et.al. studied high-entropy-stabilized chalcogenides with thermoelectric performance and conducted high-angle annular dark field (HAADF) and atomic X-ray EDS analysis using STEM at different scales and in different areas to investigate the homogeneity, finding that the distribution of all elements was homogeneous from the *micrometer to nanometer scales*.[31] In the same work, the authors claimed that, although XRD analysis showed the macroscopic existence of lattice

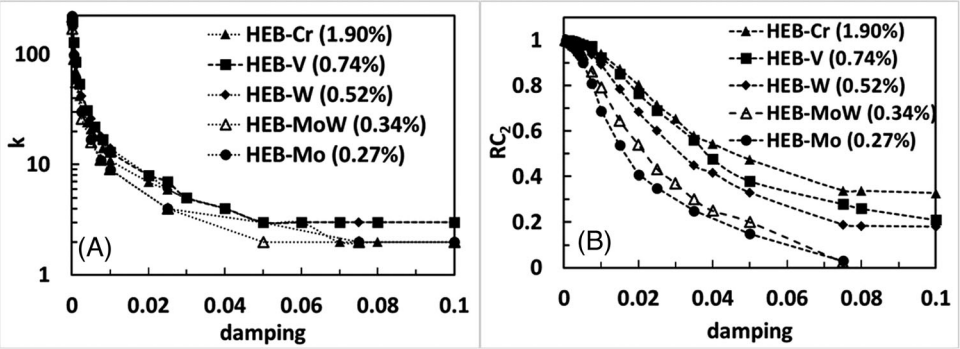

FIGURE 10 Variation of the k value of unreplicated δ_{TM} values isolated in the map of 225 SQBs (A), and smoothness of the chemical homogeneity (RC_2) varying the damping from 10^{-4} to 0.1 of the δ_{TM} data. The material's legend reminds the average lattice μ-strain

strains, the type and statistical/spatial distributions were not able to be discerned. Atom probe tomography (APT) was used by Chellai et al.[32] to investigate the homogeneity of high-entropy oxide nanopowders, confirming that the cations were distributed homogeneously at atomic level. Unfortunately, no prior work has examined the homogeneity of TMs in high entropy borides.

To address this lack of knowledge, the present work systematically tackled the subject of the chemical distribution of TMs using a combination of FESEM-EDS analysis and measurement of the lattice μ-strain. While μ-strain provides average information about the lattice disomogeneities occurring in the whole (bulk) sample and for X-rays is particularly ascribed to the TMs (rather than lighter elements), analytical FESEM-EDS with sufficient spatial resolution typically probes chemical homogeneity at scales of a few tenths of microns. Conventional FESEM-EDS chemical analysis can thus supply compositional information at the microscale within single grains, but it does not provide information at the nanoscale such as the local chemical environment or local lattice distortions around the individual anions/cations. This problem can be addressed, in part, using X-ray absorption spectroscopy (XAS) in the near-edge region (XANES). For example, Fracchia et al.[33] reported the chemical homogeneity and purity of a single phase $(Co,Mg,Mn,Ni,Zn)(Al,Co,Cr,Fe,Mn)_2O_4$ spinel ceramic (space group $Fd\bar{3}m$) through a combination of X-ray diffraction, high resolution transmission electron microscopy, and energy dispersive X-ray spectroscopy. One notable outcome was the confirmation of a partial degree of inversion in the spinel structure from analysis of the pre-edge XAS peaks from all of the cations.

Most HEB studies have dealt with starting compositions with equimolar ratios of the TMs and have assumed that the HEBs maintained the nominal composition after synthesis and sintering. However, a few have reported chemical compositions that deviate from equimolarity. To the best of our knowledge, none argued that fluctuations in the long-range chemical composition were present after sintering, without producing coherent clustering or phase separation (i.e., identifying a second phase). In this respect, Nb (i.e., HEB-Nb) may or not be a special case. The densification curves in Figure 3 demonstrate that Nb reduces mobility in the system compared to the other TMs (Ti, Ta, Zr, and Hf), which inhibited densification of the HEB-Nb and produced microstructures with long-range clustering (see Figure 2) that were obvious in SEM analysis. Rietveld refinement of high-resolution SR-XRPD pattern did not reveal the presence of a second (clustered) phase, which led to the conclusion that any Nb- segregation within the main $(Ti,Ta,Nb,Zr,Hf)B_2$ solid solution was either below the detection threshold of SR-XRPD (i.e., less than 0.5 wt%) or had the same lattice parameters as the dominant phase. Unfortunately, the statistical method to track the chemical texture could not be applied because the requirement of single phase was not fulfilled for HEB-Nb. More details about the non-uniformity of Nb and other TMs in HEB-Nb is shared in Supporting information. Apart from HEB-Nb, the other materials listed in Table 1 were found to consist of a single phase with mean grain sizes ranging from about 3 μm (HEB-Cr) up to 16 μm (HEB-Mo). This allowed us to apply the above-described FESEM-EDS chemical analysis based on measurement of dozens of grains. The correlation between increasing chemical fluctuations ($\sigma_{\delta TM}$) and larger average lattice μ-strains suggests a relationship between the two characteristics. Two different sintering temperatures, 2100°C and 2000°C, were selectively applied to two sub-groups of compositions to: i) obtain a single-phase material; ii) reach near full density; and iii) limit grain coarsening. This approach produced dense and single phase sintered AlB_2-type solid solutions, some of which had chemical inhomogeneity that manifested itself as subtle rippling of the relative contents of various TMs randomly varying around the average values. The sensitivity and resolution of SR-XRPD together with FESEM-EDS

mapping were able to capture these features. The chemical inhomogeneity and its final extent are not an intrinsic property of the material, but mainly result from the processing history, which suggests that the route to synthesize the starting mixed diboride powders may influence the final chemical homogeneity of the sintered material. The powder mixtures used for SPS listed in Table 1, for instance, were produced by boro/carbothermal reduction of mixed oxides.[11] The result was mixtures of different diboride solid solutions, the sinterability of which depended on the purity, composition, and particle size distribution. In the present case, compositions that could be fully densified at 2000°C (i.e., HEB-Mo and HEB-MoW) had enhanced mobility of the TMs and were chemically homogeneous. As a result, lattice μ-strain (see Table 1) and LRCF values (see Figure 7) were the lowest among the as-sintered materials. Conversely for the HEB-Cr composition, a terminal dwell of 10 min at 2000°C was sufficient for full densification but did not produce a homogeneous distribution of TMs. As a result, HEB-Cr had the largest <Lμ-S> coupled to the strongest long-range chemical fluctuations ($\sigma_{\delta TM}$).

The texture analysis, obtained by processing the distributions of δ_{TM}, were further proof of chemical fluctuations. Not only these fluctuations exist, but they possess specific intensities and vary across the grains. More extreme sintering conditions, for example, by extending the isothermal dwell at 2100°C or increasing the peak temperature, will likely decrease the chemical fluctuations and randomize the long-range mixing of the TMs. The present work provides a non-destructive analytical tool to detect and determine the degree of randomization of the principal species used to produce complex multi-element crystalline phases and can be easily extended to other classes of HE ceramic materials.

5 | CONCLUSION

The chemical homogeneity in high-entropy ceramics was investigated for the AlB_2-type class of multi-metal diborides. The combination of high-resolution powder diffraction profile analysis and SEM-EDS elemental mapping enabled the disclosure of the chemical distribution of transition metals within the single grains and across larger areas. In the investigated samples, lattice μ-strain which originates from a non-negligible distribution of cell parameters across microscopic distances, positively correlates with the chemical distribution of transition metal species found by elemental mapping. In particular, larger lattice μ-strain values matched with the increasing inhomogeneity in the SEM-EDS elemental maps, and this variation was quantified empirically. Those compositions that exhibited faster densification rates also displayed the highest degree of randomization, minimizing the final lattice μ−strain. The method presented herein can be broadly applied to other classes of chemically-disordered crystalline materials.

ACKNOWLEDGMENTS

The authors are grateful to Elettra-Sincrotrone Trieste for providing beamtime and financial support for the SR-XRPD experiment (proposal number 20200101). The effort of L. Feng, W. Fahrenholtz, and G. Hilmas was supported by the U.S. National Science Foundation through grant CMMI-1902069. Open Access Funding provided by Consiglio Nazionale delle Ricerche within the CRUI-CARE Agreement.

ORCID

William Fahrenholtz https://orcid.org/0000-0002-8497-0092

REFERENCES

1. Sun Y, Dai S. High-entropy catalysts: supremacy of diversity. Chem Catal. 2021;1(3):490–492. https://doi.org/10.1016/j.checat.2021.06.019
2. Xiang H, Xing Y, Dai F, Wang H, Su L, Miao L, et al. High-entropy ceramics: present status, challenges, and a look forward. J Adv Ceram. 2021;10(3):385–441. https://doi.org/10.1007/s40145-021-0477-y
3. Zhang R-Z, Reece MJ. Review of high entropy ceramics: design, synthesis, structure and properties. J Mater Chem A. 2019;7(39):22148–22162. https://doi.org/10.1039/C9TA05698J
4. Akrami S, Edalati P, Fuji M, Edalati K. High-entropy ceramics: review of principles, production and applications. Mater Sci Eng R Reports. 2021;146:100644. https://doi.org/10.1016/j.mser.2021.100644
5. Wright AJ, Luo J. A step forward from high-entropy ceramics to compositionally complex ceramics: a new perspective. J Mater Sci. 2020;55(23):9812–9827. https://doi.org/10.1007/s10853-020-04583-w
6. Cantor B, Chang ITH, Knight P, Vincent AJB. Microstructural development in equiatomic multicomponent alloys. Mater Sci Eng A. 2004;375–377(1-2 SPEC. ISS):213–218. https://doi.org/10.1016/j.msea.2003.10.257
7. Rost CM, Sachet E, Borman T, Moballegh A, Dickey EC, Hou D, et al. Entropy-stabilized oxides. Nat Commun. 2015;6:8485. https://doi.org/10.1038/ncomms9485
8. Gild J, Zhang Y, Harrington T, Jiang S, Hu T, Quinn MC, et al. High-entropy metal diborides: a new class of high-entropy materials and a new type of ultrahigh temperature ceramics. Sci Rep. 2016;6(1):37946. https://doi.org/10.1038/srep37946
9. Oses C, Toher C, Curtarolo S. High-entropy ceramics. Nat Rev Mater. 2020;5(4):295–309. https://doi.org/10.1038/s41578-019-0170-8
10. Feng L, Fahrenholtz WG, Brenner DW. High-entropy ultra-high-temperature borides and carbides: a new class of materials for extreme environments. Annu Rev Mater Res. 2021;51(1):165–185. https://doi.org/10.1146/annurev-matsci-080819-121217

11. Feng L, Monteverde F, Fahrenholtz WG, Hilmas GE. Superhard high-entropy AlB2-type diboride ceramics. Scr Mater. 2021;199:113855. https://doi.org/10.1016/j.scriptamat.2021.113855
12. Cantor B. Multicomponent high-entropy Cantor alloys. Prog Mater Sci. 2021;120:100754. https://doi.org/10.1016/j.pmatsci.2020.100754
13. Luo SC, Guo WM, Plucknett K, Lin HT. Fine-grained dual-phase high-entropy ceramics derived from boro/carbothermal reduction. J Eur Ceram Soc. 2021;41(6):3189–3195. https://doi.org/10.1016/j.jeurceramsoc.2020.12.044
14. Zhang Y, Jiang Z-B, Sun S-K, Guo W-M, Chen Q-S, et al. Microstructure and mechanical properties of high-entropy borides derived from boro/carbothermal reduction. J Eur Ceram Soc. 2019;39(13):3920–3924. https://doi.org/10.1016/j.jeurceramsoc.2019.05.017
15. Gu J, Zou J, Sun S-K, Wang H, Yu Su-Y, Zhang J, et al. Dense and pure high-entropy metal diboride ceramics sintered from self-synthesized powders via boro/carbothermal reduction approach. Sci China Mater. 2019;62(12):1898–1909. https://doi.org/10.1007/s40843-019-9469-4
16. Feng L, Fahrenholtz WG, Hilmas GE, Monteverde F. Effect of Nb content on the phase composition, densification, microstructure, and mechanical properties of high-entropy boride ceramics. J Eur Ceram Soc. 2021; 825:141741. https://doi.org/10.1016/j.jeurceramsoc.2020.08.058
17. Gild J, Wright A, Quiambao-Tomko K, Qin M, Tomko JA, bin Hoque MdS, et al. Thermal conductivity and hardness of three single-phase high-entropy metal diborides fabricated by borocarbothermal reduction and spark plasma sintering. Ceram Int. 2020;46(5):6906–6913. https://doi.org/10.1016/j.ceramint.2019.11.186
18. Zhang Y, Sun S-K, Guo W-M, Zhang W, Xu L, Yuan J-H, et al. Fabrication of textured (Hf0.2Zr0.2Ta0.2Cr0.2Ti0.2)B2 high-entropy ceramics. J Eur Ceram Soc. 2021;41(1):1015–1019. https://doi.org/10.1016/j.jeurceramsoc.2020.08.071
19. Qin M, Gild J, Wang H, Harrington T, Vecchio KS, Luo J. Dissolving and stabilizing soft WB2 and MoB2 phases into high-entropy borides via boron-metals reactive sintering to attain higher hardness. J Eur Ceram Soc. 2020;40(12):4348–4353. https://doi.org/10.1016/j.jeurceramsoc.2020.03.063
20. Qin M, Gild J, Hu C, Wang H, Bin Hoque MdS, Braun JL, et al. Dual-phase high-entropy ultra-high temperature ceramics. J Eur Ceram Soc. 2020;40(15):5037–5050. https://doi.org/10.1016/j.jeurceramsoc.2020.05.040
21. Zhang Y, Guo W-M, Jiang Z-B, Zhu Qi-Qi, Sun S-K, You Y, et al. Dense high-entropy boride ceramics with ultra-high hardness. Scr Mater. 2019;164:135–139. https://doi.org/10.1016/j.scriptamat.2019.01.021
22. Zhang Y, Sun S-K, Zhang W, You Y, Guo W-M, Chen Z-W, et al. Improved densification and hardness of high-entropy diboride ceramics from fine powders synthesized via borothermal reduction process. Ceram Int. 2020;46(9):14299–14303. https://doi.org/10.1016/j.ceramint.2020.02.214
23. Liu D, Liu H, Ning S, Ye B, Chu Y. Synthesis of high-purity high-entropy metal diboride powders by boro/carbothermal reduction. J Am Ceram Soc. 2019;102(12):7071–7076. https://doi.org/10.1111/jace.16746
24. Ma M, Ye B, Han Y, Sun L, He J, Chu Y. High-pressure sintering of ultrafine-grained high-entropy diboride ceramics. J Am Ceram Soc. 2020;103(12):6655–6658. https://doi.org/10.1111/jace.17387
25. Monteverde F, Saraga F, Gaboardi M, Plaisier JR. Compositional pathways and anisotropic thermal expansion of high-entropy transition metal diborides. J Eur Ceram Soc. 2021;41(13):6255–6266. https://doi.org/10.1016/j.jeurceramsoc.2021.05.053
26. Pecharsky VK, Zavalij PY. Fundamentals of powder diffraction and structural characterization of materials. Boston, MA: Springer US; 2009 https://doi.org/10.1007/978-0-387-09579-0
27. Feng L, Fahrenholtz WG, Hilmas GE. Two-step synthesis process for high-entropy diboride powders. J Am Ceram Soc. 2020;103(2):724–730. https://doi.org/10.1111/jace.16801
28. Toby BH, Von Dreele RB. GSAS-II : the genesis of a modern open-source all purpose crystallography software package. J Appl Crystallogr. 2013;46(2):544–549. https://doi.org/10.1107/S0021889813003531
29. ASTM A. C373 Standard test method for water absorption, bulk density, apparent porosity, and apparent specific gravity of fired whiteware products, vol. 88, no. 1999.
30. Haralick RM, Dinstein I, Shanmugam K. Textural features for image classification. IEEE Trans Syst Man Cybern. 1973;SMC-3(6):610–621. https://doi.org/10.1109/TSMC.1973.4309314
31. Jiang B, Yu Y, Cui J, Liu X, Xie L, Liao J, et al. High-entropy-stabilized chalcogenides with high thermoelectric performance. Science. 2021;371(6531):830–834. https://doi.org/10.1126/science.abe1292
32. Chellali MR, Sarkar A, Nandam SH, , Bhattacharya SS, Breitung B, Hahn H, et al. On the homogeneity of high entropy oxides: an investigation at the atomic scale. Scr Mater. 2019;166:58–63. https://doi.org/10.1016/j.scriptamat.2019.02.039
33. Fracchia M, Manzoli M, Anselmi-Tamburini U, Ghigna P. A new eight-cation inverse high entropy spinel with large configurational entropy in both tetrahedral and octahedral sites: synthesis and cation distribution by X-ray absorption spectroscopy. Scr Mater. 2020;188:26–31. https://doi.org/10.1016/j.scriptamat.2020.07.002

SUPPORTING INFORMATION

Additional supporting information can be found online in the Supporting Information section at the end of this article.

How to cite this article: Monteverde F, Saraga F, Gaboardi M, Feng L, Hilmas G, Fahrenholtz W. Quantitative inspection of grain-scale chemical inhomogeneities in high-entropy AlB_2-type transition metal diborides. J Am Ceram Soc. 2022;1–14. https://doi.org/10.1111/jace.18619